Open Research Online

Observations of the *Hubble Deep Field* with the *Infrared Space Observatory* - II. Source detection and photometry

Journal Item

For guidance on citations see FAQs.

Version: Version of Record

Link(s) to article on publisher's website:
http://dx.doi.org/doi:10.1093/mnras/289.2.465
http://dx.doi.org/10.1093/mnras/289.2.465

oro.open.ac.uk

Observations of the *Hubble Deep Field* with the *Infrared Space Observatory* – II. Source detection and photometry

P. Goldschmidt,[1] S. J. Oliver,[1] S. B. G. Serjeant,[1] A. Baker,[2] N. Eaton,[1]
A. Efstathiou,[1] C. Gruppioni,[1] R. G. Mann,[1] B. Mobasher,[1] M. Rowan-Robinson,[1]
T. J. Sumner,[1] L. Danese,[3] D. Elbaz,[2] A. Franceschini,[4] E. Egami,[5] M. Kontizas,[6]
A. Lawrence,[7] R. McMahon,[8] H. U. Norgaard-Nielsen,[9] I. Perez-Fournon[10] and
J. I. Gonzalez-Serrano[11]

[1]*Astrophysics Group, Imperial College London, Blackett Laboratory, Prince Consort Road, London SW7 2BZ*
[2]*Service d'Astrophysique, Saclay, 91191, Gif-sur-Yvette Cedex, France*
[3]*SISSA, Via Beirut 2-4, Trieste, Italy*
[4]*Osservatorio Astronomico di Padova, Vicolo dell'Osservatorio 5, I-35, 122, Padova, Italy*
[5]*Max-Planck-Institut für Extraterrestrische Physik, Giessenbachstrasse, D-8046, Garching bei Munchen, Germany*
[6]*Astronomical Institute, National Observatory of Athens, PO Box 200048, GR-118 10, Athens, Greece*
[7]*Institute for Astronomy, University of Edinburgh, Blackford Hill, Edinburgh EH9 3HJ*
[8]*Institute of Astronomy, The Observatories, Madingley Road, Cambridge CB3 0HA*
[9]*Danish Space Research Institute, Gl. Lundtoftevej 7, DK-2800 Lyngby, Copenhagen, Denmark*
[10]*Instituto de Astrofisica de Canarias, Via Lactea, E-38200 La Laguna, Tenerife, Canary Islands, Spain*
[11]*Instituto de Fisica de Cantabria, Santander, Spain*

ABSTRACT

We present positions and fluxes of point sources found in the *Infrared Space Observatory* (*ISO*) images of the *Hubble Deep Field* (HDF) at 6.7 and 15 μm. We have constructed algorithmically selected 'complete' flux-limited samples of 19 sources in the 15-μm image, and seven sources in the 6.7-μm image. The typical flux limit at 15 μm is ~ 0.2 mJy and at 6.7 μm is ~ 0.04 mJy. We have selected 'supplementary' samples of three sources at 15 μm and 20 sources at 6.7 μm by eye. We discuss the completeness and reliability of the connected pixel source detection algorithm used, by comparing the intrinsic and estimated properties of simulated data, and also by estimating the noise properties of the real data. The most pessimistic estimate of the number of spurious sources in the 'complete' samples is one at 15 μm and two at 6.7 μm, and in the 'supplementary' lists is one at 15 μm and five at 6.7 μm.

Key words: surveys – infrared: galaxies.

1 INTRODUCTION

The *Hubble Deep Field* (HDF: Williams et al. 1996) consists of ~ 3 square arcminutes near the North Galactic Pole that has been surveyed by the *Hubble Space Telescope* (*HST*) in four wavebands (approximating to U, B, V, I) to an average limiting magnitude of $m \sim 28$. We have surveyed this area with the *Infrared Space Observatory* (*ISO*: Kessler et al. 1996) using the ISOCAM instrument (Cesarsky et al. 1996) at 6.7 and 15 μm. This paper, the second in a series which presents and discusses the *ISO* data, addresses the problem

of source detection and photometry. Data acquisition and construction of these images are described in more detail in Paper I by Serjeant et al. (1997). We briefly summarize the steps taken to reduce the data below.

Section 2 of this paper discusses the results of running the object detection algorithm on the data and presents tables of detected objects with their positions and fluxes. Section 3 discusses how data were simulated to test the completeness and reliability of the object detection algorithm and the photometry.

© 1997 RAS

2   DETECTED OBJECTS AND THEIR ESTIMATED FLUXES

Paper I describes the strategy behind the data acquisition and construction of the images used in this paper. We briefly summarize the main steps of data acquisition and reduction here. In order to increase the spatial resolution of the resulting images, *ISO* was used in a microscanning mode and rasters were made with fractional pixel offsets between each raster centred on each HDF Wide Field (WF) frame. The default dark frame was subtracted from the data, which were then deglitched by identifying and masking our cosmic ray events in the pixel histories. Flat-fields were created by using the mean sky value measured by each pixel; this method assumes no significant contamination from genuine objects which would bias the flat-field. Cosmic ray events were filtered out in the time domain, by excluding all 4σ events. Longer term effects such as glitch transients, which could mimic objects, were filtered out at each position using slightly different techniques at each wavelength. The most obvious way to exclude glitches is to median-filter the data at each pointing; however, this results in lower signal-to-noise ratio than does a simple mean. It was decided to mosaic the rasters together using the same 'drizzling' routine with which the optical HDF images were created. This meant that the mean of each pointing was taken, pointings with integer pixel offsets were 'medianed' together, and then the resulting 'medianed' images were drizzled together. The original pixel sizes were 3 and 6 arcsec at 6.7 and 15 μm respectively. After running the drizzling algorithm, the final sizes were 1 and 3 arcsec at 6.7 and 15 μm respectively.

2.1   The source detection algorithm

We used the object detection algorithm PISA, which counts contiguous pixels above a user-supplied threshold (Draper & Eaton 1996). If the number of contiguous pixels exceeds a user-supplied minimum, then these pixels are defined as being an object. The minimum number of contiguous pixels that a detected object must have is set by considering the number of pixels in the point spread function, and also from tests with simulated data.

PISA uses a constant threshold per pixel across each image, and this threshold depends on the noise; therefore before running PISA we split the image up into sub-images, according to the noise level. We estimated the noise per pixel by looking at the variance from all the different pixels that had contributed to each pixel in the final drizzled image. This variance was dominated by Poisson statistics: the area on the sky that was sampled most by all three overlapping images had the lowest variance, and the edges which were sampled by the fewest pixels had the highest variance. As mentioned above, there was so much overlap between the three fields making up the 15-μm image that we decided to create two sub-images of this image: one for the edges which had high variance and one for the rest of the image which had much lower variance. For the 6.7-μm image, the overlap region was smaller, and we created three sub-images with different noise values: the central overlap region, the surrounding region of the individual fields and the edges.

For the 15-μm image the detection criterion was as follows: each pixel had to have a flux greater than 2σ above the modal sky value in that region, where σ was estimated from the variance in the sky counts and also from the pixel history. The two estimates of σ are in good agreement with each other. The minimum number of contiguous pixels in a detected object was set to be 8. Running PISA produced 19 objects in the 15-μm image, using the input values in Table 1.

2.2   Photometry of detected sources

Although PISA estimates total fluxes for detected objects, it was decided to use a different estimator for the fluxes of the objects. The images appear to be confusion-limited (Paper I), and therefore a constant sky value is not a good estimate of the local background if we are trying to estimate the excess flux due to objects in faint pixels.

A better, although not perfect, method is to measure the local sky, using a concentric annulus around the aperture selected to estimate the flux of the object. This is still not ideal, since the sky brightness in confusion-limited images fluctuates on spatial scales similar to the size of the objects. Therefore the sky adjacent to an object may not be a good estimate of the sky at the position of the object. A radius of 12 arcsec for the aperture was chosen because this radius encircles 96 per cent of the empirically determined point spread function (Oliver et al. 1997, hereafter Paper III). The sky annulus had an inner radius of 15 arcsec and an outer radius of 24 arcsec. Ideally, a large sky annulus is preferable if the noise is random, but because of the spatial variations in the sky one needs as 'local' a value for the sky as possible.

In the next section we describe how we simulate data to estimate errors and completeness as a function of flux. Here we describe how we used the real images to estimate the errors at each wavelength. We created 'sky maps' by convolving the sky annulus with each image to give the estimated sky value at each pixel. We then subtracted this from the original image and convolved the resulting image with the object aperture. This image has, at each pixel, an estimate of the 'object-minus-sky' flux that a detected object would have if it were centred on that image. The variance in this resulting image therefore gives the variance in the fluxes of the estimated objects. We find that at 15 μm the 1σ error is ~ 0.1 mJy and at 6.7 μm it is 0.02 mJy. This is a conservative overestimate of the noise, since we have made no attempt to mask our genuine objects which presumably will increase the measured variance. However, these noise estimates do agree with those estimated from simulated data as discussed below.

Table 1. The sky and threshold intensities in mJy arcsec^{-2} used to select objects in the two sub-images of the 15-μm image.

Name	Sky	Threshold
Area 1	0.402	7.6×10^{-4}
Area 2	0.402	1.6×10^{-3}

For each object detected at 15 μm, aperture photometry was performed at the same position in the 6.7-μm image in order to determine the flux at that wavelength. The measured flux at 6.7 μm was designated as a detection if it was more than the estimated detection limit at that position. This detection limit was derived by assuming that the objects are not resolved and therefore, given the PISA criteria, one can calculate the total flux of an object from knowing the point spread function (see Paper III for more details). Many 15-μm sources are outside the area of the 6.7-μm image, and thus do not have upper limits at 6.7 μm. Table 2 lists the positions, fluxes at 15 μm and upper limits at 6.7 μm estimated for each object detected in the 15-μm field. Section 3 discusses error estimates of the measured fluxes, using simulated data.

In principle, conversion of the instrumental counts to flux densities is straightforward, since ISOCAM is a linear device, and involves a constant transformation at all fluxes. However, this assumes that the total on-source integration time is long enough to reach stabilization. Pre-flight tests suggest that instrumental units should be converted to flux densities in units of mJy by dividing by M, where $M = 2.19$ at 6.7 μm and $M = 1.96$ at 15 μm (ISO-CAM Observer's Manual 1994). Subsequently, in-flight data have indicated that this value of M should be changed to correct for 'point source flux loss'. We therefore use $M = 1.93$ at 6.7 μm and $M = 1.57$ at 15 μm: these are the values recommended by the CAM instrumental team. Additionally, the instrument does

not always reach stabilization, and typically the first readout measures ~60 per cent of the flux of an object. If this is the case, then M should be further multiplied by 0.6. However, we are not sure that this further correction to M applies to our data, and have therefore not used it. It should be borne in mind that the fluxes we present in Tables 2, 3, 5 and 6 are preliminary.

In addition, a number of objects were selected by PISA with slightly less stringent criteria. This meant that a higher number of spurious objects were selected. A slightly lower threshold was used in the selection, and the resulting objects were 'eyeballed' to see whether they looked genuine. This is because PISA chooses connected pixels regardless of shape, i.e. a chain of connected pixels above the threshold will be selected as an object in the same way as a circle of pixels. Eyeballing these selected objects therefore was designed to select the 'round' objects that appeared to have the sort of smooth profiles that one would expect a genuine object convolved with the point spread function to have. These objects will be referred to in this and subsequent papers as the supplementary objects. Mann et al. (1997, Paper IV) discuss the likelihood of these objects being genuine by matching them up to the optical HDF image. Note that these objects are *not* selected with any reference to the optical images.

Table 3 lists the positions and fluxes of these objects. Because the criteria by which these objects were selected is not fully algorithmic and limiting fluxes cannot be estimated

Table 2. Names, positions, estimated fluxes and upper limits at 6.7 μm in mJy, for objects selected from the 15-μm image by PISA. Objects that fall outside the 6.7-μm image are represented by '-'.

Name	RA (2000)	dec (2000)	flux	flux at 6.7 μm
ISOHDF3 J123633.9+621217	12 36 33.96	+62 12 17.8	0.7263	-
ISOHDF3 J123634.3+621238	12 36 34.37	+62 12 38.6	0.4442	-
ISOHDF3 J123635.9+621134	12 36 35.95	+62 11 34.7	0.4196	-
ISOHDF3 J123636.5+621348	12 36 36.54	+62 13 48.4	0.6490	-
ISOHDF3 J123637.5+621109	12 36 37.56	+62 11 09.6	0.2553	-
ISOHDF3 J123639.3+621250	12 36 39.33	+62 12 50.3	0.4333	<0.0975
ISOHDF3 J123641.1+621129	12 36 41.11	+62 11 29.9	0.3763	<0.0895
ISOHDF3 J123643.7+621255	12 36 43.73	+62 12 55.6	0.3186	<0.0432
ISOHDF3 J123646.9+621045	12 36 46.98	+62 10 45.3	0.4119	-
ISOHDF3 J123648.1+621432	12 36 48.13	+62 14 32.0	0.2310	0.0498
ISOHDF3 J123649.8+621319	12 36 49.88	+62 13 19.9	0.4715	0.0523
ISOHDF3 J123653.0+621116	12 36 53.05	+62 11 16.9	0.3265	-
ISOHDF3 J123653.6+621140	12 36 53.62	+62 11 40.4	0.1382	-
ISOHDF3 J123658.7+621212	12 36 58.71	+62 12 12.0	0.3357	<0.0891
ISOHDF3 J123659.4+621337	12 36 59.48	+62 13 37.3	0.3406	-
ISOHDF3 J123700.2+621455	12 37 00.25	+62 14 55.6	0.2908	-
ISOHDF3 J123702.5+621406	12 37 02.57	+62 14 06.1	0.3322	-
ISOHDF3 J123705.7+621157	12 37 05.76	+62 11 57.6	0.4718	-
ISOHDF3 J123709.8+621239	12 37 09.88	+62 12 39.1	0.5103	-

Table 3. Names, positions, estimated fluxes and upper limits at 6.7 μm in mJy, for supplementary objects selected from the 15-μm image.

Name	RA (2000)	dec (2000)	flux	flux at 6.7 μm
ISOHDF3 J123651.5+621357	12 36 51.58	+62 13 57.2	0.1549	< 0.0514
ISOHDF3 J123658.1+621458	12 36 58.12	+62 14 58.2	0.2104	-
ISOHDF3 J123702.0+621127	12 37 02.06	+62 11 27.6	0.3260	-

for them, subsequent papers (e.g. Paper III) which estimate the number counts do not use thse objects. The objects listed in Table 2 (and, for the 6.7-μm data, in Table 5) will be referred to as the complete samples.

The 6.7-μm objects were selected in the same way as the 15-μm objects. Aperture photometry was carried out using a radius of 6 arcsec and a sky annulus of width 5 arcsec and inner radius 8 arcsec. Table 4 lists the sky levels, and thresholds searched in the 6.7-μm image. Table 5 lists the objects detected by PISA in the 6.7-μm image, and Table 6 lists the objects in the supplementary catalogue. Again, we measured the fluxes of these objects at 15 μm and defined these measurements as being detections if the flux was larger than the estimated detection limit at that position.

Table 4. The sky intensities and threshold intensities in mJy arcsec^{-2} used to select objects in the three sub-images of the 6.7-μm image.

Name	sky	threshold
Area 1	0.0801	9.3×10^{-4}
Area 2	0.0802	1.1×10^{-3}
Area 3	0.0804	1.3×10^{-3}

3 TESTING THE SOURCE DETECTION ALGORITHM

PISA requires that the sky be constant across the image, down to the noise level used. In other words, we must be sky-noise-limited and not confusion-limited, at least for the brightest pixels in each object that are used to select that object. However, it is likely that the *ISO* images of the HDF are confusion-limited (Paper I; Paper III). The detectors are sensitive enough to detect faint objects, but the large telescope beam means that the flux per object is shared out between many pixels and therefore it is difficult to get an unbiased estimate of the background at the position of the detection objects.

3.1 Running the source detection algorithm on simulated data

To see whether the source detection algorithm could cope with these data, we tested it by simulating some data and running them through every stage of the source detection and photometry procedure that was used to construct the 'complete' samples.

The simulated objects were modelled by assigning flux to individual pixels. These pixels were then convolved with a

Table 5. Names, positions, estimated fluxes and upper limits at 15 μm in mJy, for objects selected from the 6.7-μm image by PISA.

Name	RA (2000)	dec (2000)	flux	flux at 15 μm
ISOHDF2 J123643.0+621152	12 36 43.05	+62 11 52.9	0.0579	<0.3362
ISOHDF2 J123646.4+621406	12 36 46.46	+62 14 06.6	0.0521	<0.3614
ISOHDF2 J123648.2+621427	12 36 48.27	+62 14 27.4	0.0657	<0.2434
ISOHDF2 J123648.4+621215	12 36 48.47	+62 12 15.3	0.0512	<0.2947
ISOHDF2 J123649.7+621315	12 36 49.78	+62 13 15.9	0.0481	0.4396
ISOHDF2 J123655.1+621423	12 36 55.19	+62 14 23.6	0.0304	<0.2682
ISOHDF2 J123658.8+621313	12 36 58.83	+62 13 13.6	0.0674	<0.2378

Table 6. Names, positions, estimated fluxes and upper limits at 15 μm in mJy, for supplementary objects selected from the 6.7-μm image.

Name	RA (2000)	dec (2000)	flux	flux at 15 μm
ISOHDF2 123641.5+621309	12 36 41.57	+62 13 09.8	0.0213	<0.1311
ISOHDF2 123641.6+621142	12 36 41.62	+62 11 42.0	0.0516	0.2646
ISOHDF2 123642.5+621256	12 36 42.50	+62 12 56.5	0.0378	0.2062
ISOHDF2 123642.6+621210	12 36 42.63	+62 12 10.9	0.0229	<0.2865
ISOHDF2 123642.9+621309	12 36 42.95	+62 13 09.2	0.0511	<0.1700
ISOHDF2 123643.1+621203	12 36 43.16	+62 12 03.6	0.0372	<0.2818
ISOHDF2 123643.9+621130	12 36 43.93	+62 11 30.0	0.0504	<0.2252
ISOHDF2 123646.6+621440	12 36 46.64	+62 14 40.2	0.0408	<0.1556
ISOHDF2 123647.1+621426	12 36 47.12	+62 14 26.5	0.0345	<0.2336
ISOHDF2 123648.6+621123	12 36 48.69	+62 11 23.2	0.0371	<0.3924
ISOHDF2 123650.2+621139	12 36 50.22	+62 11 39.1	0.0660	<0.2871
ISOHDF2 123655.2+621413	12 36 55.26	+62 14 13.9	0.0332	<0.2426
ISOHDF2 123655.7+621427	12 36 55.71	+62 14 27.0	0.0396	<0.2675
ISOHDF2 123656.1+621303	12 36 56.19	+62 13 03.1	0.0373	<0.2592
ISOHDF2 123656.6+621307	12 36 56.66	+62 13 07.3	0.0313	<0.2595
ISOHDF2 123657.4+621414	12 36 57.40	+62 14 14.0	0.0381	<0.2434
ISOHDF2 123657.6+621205	12 36 57.61	+62 12 05.7	0.0275	<0.1948
ISOHDF2 123658.6+621309	12 36 58.64	+62 13 09.3	0.0345	<0.2672
ISOHDF2 123658.9+621248	12 36 58.93	+62 12 48.1	0.0431	<0.2788
ISOHDF2 123701.2+621307	12 37 01.24	+62 13 07.8	0.0618	<0.2858

Gaussian point spread function. The resulting objects were then laid down on an image consisting of a patch of 'clean' sky from the real image. PISA was then run on this and aperture photometry was performed on the detected objects, as discussed above. The criteria by which PISA was judged to have worked were (i) the fraction of true objects detected, and (ii) the fraction of spurious objects. We also estimated the accuracy of the resulting photometry as a function of true flux.

At 15 μm PISA detected 70 per cent of the true objects at $S=0.225$ mJy, rising to 92 per cent at $S=0.45$ mJy. The mean difference between the estimated and true fluxes was always consistent with zero; however, the fractional rms scatter in the estimated fluxes for objects with $S<0.3$ mJy was ~50 per cent. For objects with $S\geq0.3$ mJy the fractional rms scatter decreased, and for $S\geq0.4$ mJy the error on the estimated fluxes was of the order of ~30 per cent. See Fig. 1 for more details of the results of the simulations. The maximum fraction of spurious objects found by PISA was ~1 per cent (three spurious objects) in 10 simulations; in other words, this implies that 0.3 objects are spurious on
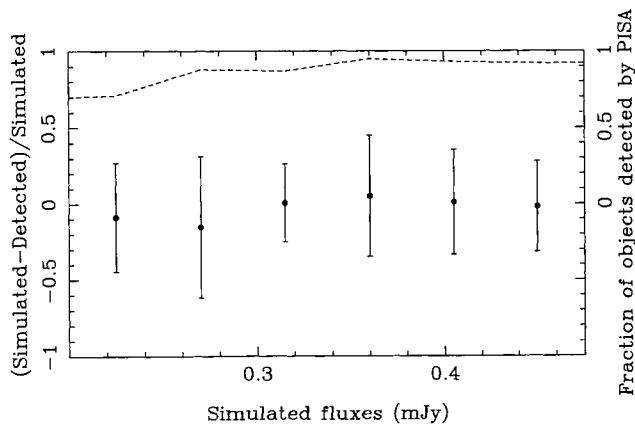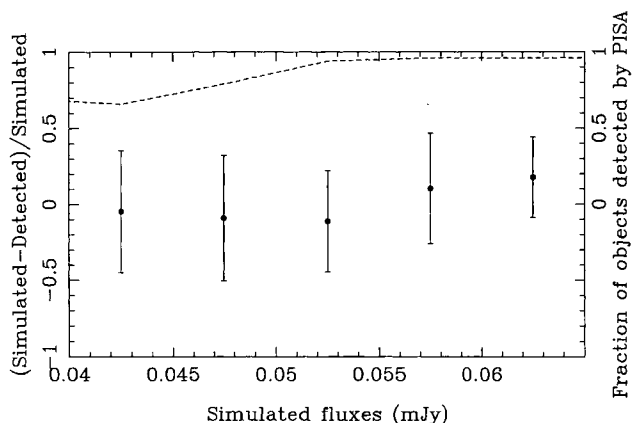
the real 15-μm image. At 6.7 μm the fraction of detected objects rose from 68 per cent at 0.04 mJy to 93 per cent at 0.065 mJy. The fractional rms error in the estimated fluxes was ~40 per cent at $S=0.0425$ mJy and decreased to ~25 per cent at $S=0.0625$ mJy. See Fig. 2 for details of the results of the simulations. The number of spurious objects found was two in seven simulations, and so we expect that, again, 0.3 objects detected are spurious.

We can test the PISA algorithm in two other ways. We can look at the number of 'negative' objects that PISA finds, i.e. the number of objects that satisfy the criteria and where each pixel is *less* than the mean sky minus the threshold. This allows us to quantify the number of random fluctuations that appear as objects. On the 15-μm image PISA detects one negative object, and on the 6.7-μm image PISA detects two negative objects. However, this is not an ideal test as the noise is not likely to be Gaussian.

Secondly, we can use the 'noise' maps to search for objects. As discussed in Paper I, these maps were created by randomizing the positions of the pixels. Therefore any real objects will be scrambled and will no longer be made up of contiguous pixels. However, noisy pixels which might be spuriously detected as real objects by PISA will still be present in these noise maps, and we can therefore try to quantify what fraction of our detections are due to noise by running PISA on the noise maps. PISA finds two objects at 6.7 μm and one object at 15 μm.

To summarize, we estimate that, at worst, one object at 15 μm and two objects at 6.7 μm in the 'complete' lists are spurious detections, and, at best, less than one object at each wavelength is spurious.

We then tested the likelihood of objects in the 'supplementary' sample being spurious. We did this by searching for sources on the 'noise' maps. This is more problematic, as it involves human selection 'by eye' and thus relies on this part of the selection being fully reproducible and also unbiased by the knowledge that there are no 'true' objects on these maps. A pessimistic estimate is that one object at 15 μm and five objects at 6.7 μm in the supplementary lists are spurious. Mann et al. (1997, Paper IV) address this issue further by matching objects detected in this paper to optically selected galaxies in the HDF.

Figure 1. The dotted line shows the fraction of simulated objects detected by PISA (right-hand axis) and the data points show the fractional errors in their estimated fluxes at 15 μm (in mJy, on the left-hand axis) as a function of flux.

4 SUMMARY

We have used a contiguous pixel algorithm to detect objects in the *ISO* images of the HDF and flanking fields. We have presented tables of objects found at both 15 and 6.7 μm. These are the faintest objects ever discovered at these wavelengths. We estimate from the data that the errors on the measured fluxes are ~0.1 mJy (~30 per cent) at 15 μm and ~0.02 mJy (~40 per cent) at 6.7 μm. Using simulated data on a real image of the sky, we estimate that, down to a flux limit of 0.045 mJy at 6.7 μm and 0.225 mJy at 15 μm, PISA can detect ≥75 per cent of known objects. Also using this simulated data, the relative errors in the estimated photometry of these objects are ~20–50 per cent. The simulated data imply that there is less than one spurious source at both 15 and 6.7 μm, whereas using PISA on the noise maps, and counting the number of negative sources, implies that 1–2 objects at each of the wavelengths might be spurious in the complete samples.

Figure 2. The dotted line shows the fraction of simulated objects detected by PISA (right-hand axis) and the data points show the fractional errors in their estimated fluxes at 6.7 μm (in mJy, on the left-hand axis) as a function of flux.

Further information on the *ISO* HDF project can be found on the *ISO* HDF WWW pages (http://artemis.ph.ic.ac.uk/hdf/).

ACKNOWLEDGMENTS

This paper is based on observations with *ISO*, an ESA project with instruments funded by ESA member states (especially the PI countries: France, Germany, the Netherlands and the United Kingdom) and with the participation of ISAS and NASA. We thank the referee, Leo Metcalfe, for helpful and informative comments. Data reduction was partially carried out on Starlink. This work was supported by PPARC grant GR/K98728 and by the EC TMR Network programme, FMRX-CT96-0068.

REFERENCES

Cesarsky C. et al., 1996, A&A, 315, 32
Draper P. W., Eaton N., 1996, pisa Starlink User Note 109 (http://star-www.rl.ac.uk/star/docs/sun109.htx/sun109.html)
ISO-CAM Observer's Manual, version 1.0, 1994, ESA/ESTEC
Kessler M. et al., 1996, A&A, 315, 27
Mann R. G. et al., 1997, MNRAS, 289, 482 (Paper IV, this issue)
Oliver S. J. et al., 1997, MNRAS, 289, 471 (Paper III, this issue)
Serjeant S. et al., 1997, MNRAS, 289, 457 (Paper I, this issue)
Williams R. E. et al., 1996, AJ, 112, 1335